Development of a Dielectric-Gas-Based Single-Phase Electrostatic Motor

Nannan Zhao [ID], Zihao Song, Zhengxu Li, Nuo Shi, Fei Lu [ID], *Member, IEEE*, Hua Zhang [ID], *Member, IEEE*,
Chris Mi [ID], *Fellow, IEEE*, and Weiguo Liu, *Senior Member, IEEE*

Abstract—**Electrostatic motor can work as a supplement to the electromagnetic motor due to its simple structure, low cost, light weight, and high efficiency. This paper presents a dielectric-gas-based single-phase electrostatic motor with simplified construction. The motor design is focused on increasing the capacitance, subsequently the torque, to make the electrostatic motors competitive with the electromagnetic ones. Three-dimensional (3-D) finite element analysis (FEA) simulation and optimization process of the electrostatic motor is performed. A 50 W electrostatic motor with the torque of 0.25 N·m, which is the same order in magnitude with the fluid-filled electrostatic machine and induction machine at the similar power level, is designed. Losses including the friction loss, windage loss, and dielectric loss are predicted. Thermal fields are analyzed using FEA and the electrostatic motor presented can work stably at high ambient temperature. 3-D printing is used to build a prototype machine to eliminate the process of mould manufacture and achieve a weight reduction. Predicted capacitance of machine is compared with measured result and good agreement is achieved.**

Index Terms—**Capacitance, electrostatic motor, losses, thermal, three-dimensional (3-D) printing.**

I. INTRODUCTION

ELECTROSTATIC field has many practical uses, e.g., capacitive power transfer utilizing electrostatic field can realize 150 mm wireless power transmission at high efficiency [1], [2]. Electrostatic motors are electromechanical devices utilizing electrostatic force generated by capacitive power transfer between electrodes. When power is applied to the stator electrodes, the rotor's electrical elastance creates a force that attempts to align the rotor electrodes with the nearest stator electrodes to minimize the elastance. Generally, the energy density of electrostatics is much lower than that of electromagnetics in macro scale. However, electric field strength between electrodes increases rapidly with the decrease of distance, producing comparative electrostatic force. Nowadays, electrostatic motors, especially the variable elastance electrostatic motors have been widely used in micro-electro-mechanical-systems (MEMS) [3], [4].

Compared with electromagnetic motor, electrostatic motor is constructed of dielectric and electrodes only, eliminating the costly winding, permanent magnet, and lamination core, thus the manufacture complexity and the cost of electrostatic machine can be reduced. Besides, the electric field strength between electrodes is independent of the thickness of electrode's conducting layer, hence lightweight materials can be chosen for electrodes with a thin conducting layer to decrease the weight.

Loss is one of the most important design considerations of motor since it affects efficiency and thermal field directly. Iron loss in iron core and copper loss in winding are two dominant loss of electromagnetic motor resulting in efficiency decrease and temperature rise. Conversely, there is no copper loss in electrostatic motor by eliminating the copper winding and no iron loss by eliminating the iron core and permanent magnet. Additional dielectric loss, loss of energy that goes into heating a dielectric material in a varying electric field, should be considered. However, dielectric loss takes only fractional percentage of the power in MHz class [13]. Thus, high efficiency and good thermal condition of electrostatic motor should be obtained.

Some application backgrounds demand that the motor can work stably in high temperature environment, which will cause irreversible damage to the magnets and the winding insulation of electromagnetic motor, while electrostatic motor can still operates well due to the simple structure with high-temperature endurable materials. Besides, electrostatic motor, with none magnetic materials, can be used in high-intensity magnetic field application.

Therefore, due to its simple structure, low cost, light weight, and high efficiency, electrostatic motor can work as a supplement to the electromagnetic motor, especially in the applications under high temperature conditions or sensitive to magnetic fields.

The main drawback of the electrostatic motor that restricts its development in macro scale is its relatively low value of torque, which can be improved by increasing the applied voltage under ultra-high vacuum (UHV) condition or using dielectric liquid

with high relative permittivity [5]. The UHV approach has been employed in [11] and [12]. Sensors are attached to detect the relative position between the stator electrodes and rotor electrodes. Voltages of different polarities, switched according to pre-determined timing, are applied to the electrodes on the rotor side in order to generate constant driven torque between the stator and the rotor, resulting in a single-phase electrostatic motor in a high, clean vacuum with a voltage from 1 to 100 kV, a maximum speed of 10 000 r/min, a maximum torque of 0.1 N·m, a power of 100 W, and an efficiency >95%. Progressive research work has been done in the dielectric-liquid-filled electrostatic motor. From [5]–[10], evaluation of dielectric fluids, the nature of electrostatic torque production, axial-peg-style motor topology and optimization design, capacitance and torque calculations and measurement, and three-dimensional (3-D) printing manufacture technique are discussed. A three-phase fluid-filled electrostatic rotating machine with specific torque density of 0.101 N·m/kg at 7.5 kV, comparable to the fractional horsepower class induction machine, is constructed, indicating the potential use of electrostatic machines in fluid-filled applications.

The purpose of this paper is to prove that the torque of the dielectric-gas-based electrostatic motor can reach the same order in magnitude with the fluid-filled electrostatic motor. The single-phase configuration, of which the topology and principle are much easier to understand, is first researched to validate the torque performance of the dielectric-gas-based electrostatic motor, and then transition to the three-phase configuration in the future. There are three contributions of this paper compared with previous works [5]–[12]. First, this paper presents a dielectric-gas-based single-phase electrostatic motor for low torque, low power, and high speed applications. The torque of the proposed motor can reach the same order in magnitude with the fluid-filled electrostatic motor and induction machines at the similar power level. Second, Two electric potentials of the single-phase motor are distributed on two stators respectively, thus, stator plate is no need to be insulated for different potentials, which simplifies the construction and reduces the manufacture complexity. Third, losses, including the friction loss, windage loss, and dielectric loss of the electrostatic motor, are calculated, and thermal field analysis at ambient temperature of 300 °C is performed, revealing the high-temperature endurable performance of the presented electrostatic motor.

II. MOTOR TOPOLOGY AND DESIGN

A. Motor Topology

The proposed electrostatic motor has two stators and a rotor. The stators and rotor, fitted with concentric rows of interdigitated electrodes on them, are opposed to each other in an axial direction, as shown in Fig. 1. The rotor lies in the middle of two stators, which helps to balance the axial forces between rotor and stators. Two electric potentials of the presented single-phase electrostatic motor are distributed on two stators, respectively, thus, stator plate is no need to be insulated for different potentials. Ceramic bearings are used to make sure the stators and rotor are insulating with each other. The radial force between
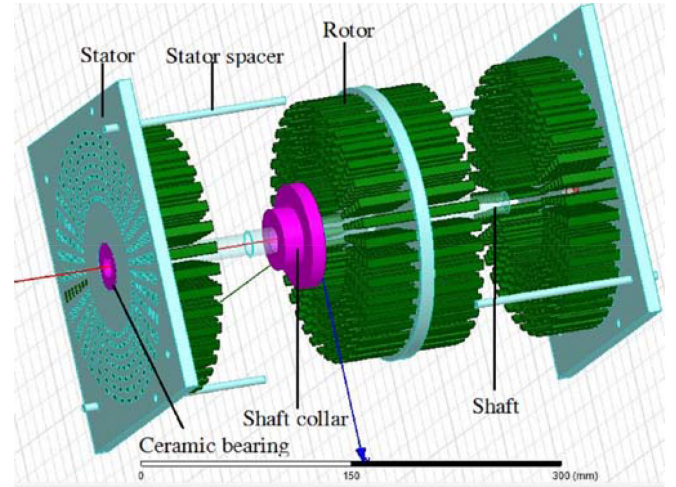

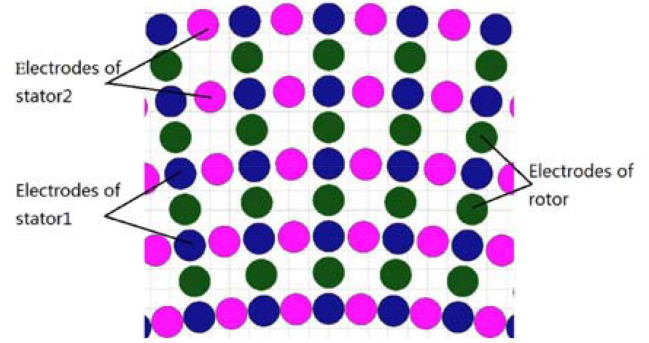Fig. 1. Assembly drawing of presented electrostatic motor.

Fig. 2. Spatial location difference of electrodes of two stators.

the rotor electrodes and stator electrodes can be derived from the term of Lorentz Force contributed by electric fields. According to [5], the torque T and capacitance C of the presented motor, considering the dynamic process of the rotor rotation and the interaction between the rotor and stator, can be derived as

$$T = V^2 \frac{\mathrm{d}}{\mathrm{d}_x} C(x)$$

$$= V^2 \frac{C_{\text{stator1}-\text{rotor}}(x) - C_{\text{stator2}-\text{rotor}}(x)}{\Delta x} \quad (1)$$

$$C(x) \propto N \frac{\varepsilon_0 \varepsilon_r s}{\mathrm{d}(x)} \quad (2)$$

where V is the applied voltage, $C_{\text{stator1}-\text{rotor}}$ is the capacitance between stator 1 and rotor, $C_{\text{stator2}-\text{rotor}}$ is the capacitance between stator 2 and rotor, x is the relative distance between the rotor electrodes and the stator electrodes, N is the number of the rotor electrodes and stator electrodes, s is the effective interaction area between the rotor and stator electrodes, and ε_0 and ε_r are vacuum permittivity and relative permittivity, respectively. According to (1), the variation of the coupling capacitance with distance should be large enough to supply adequate torque. Therefore, there is 180 electrical degrees difference between the spatial locations of electrodes for two stators, as shown in Fig. 2, which ensures a maximum capacitance variation.

TABLE I
PARAMETERS OF INITIAL DESIGN

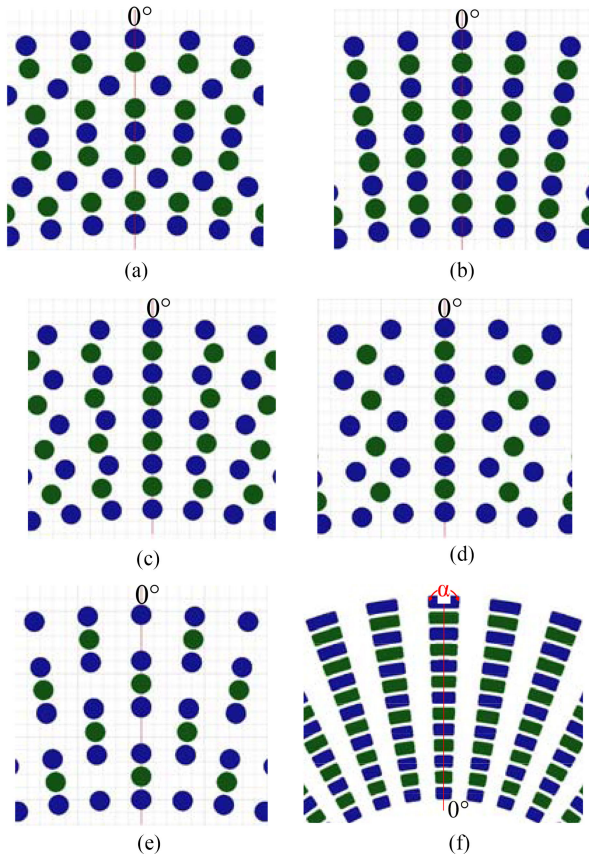| Parameters	Round electrode
Number of rows-stator	5
Number of rows-rotor	4
Electrode diameter	3.2 mm
Electrode overlapping length	25 mm
Minimum gap	0.5 mm
Row-to-row space	3.7 mm
Stator first row radius	100 mm
Stator plate outer radius	165 mm

Fig. 3. Electrodes distribution of stator 1 and rotor with different pole combination. (a) Topology_1: 96/96(1)/round/25. (b) Topology_2: 96/96(2)/round/25. (c) Topology_3: 96/80/round/25. (d) Topology_4: 96/64/round/25. (e) Topology_5: 96/48/round/25. (f) 40/40/rectangle/35.

B. Initial Design

The objective of design is to achieve the maximum capacitance variation. The cross section of electrode is firstly designed in round shape, since cylinder electrode may be available via off-the-shelf metal pin. The parameters of initial design are shown in Table I.

3-D FEA analysis is performed in Maxwell. The capacitances generated between rotor and stator with different stator pole/rotor pole combinations (stator pole/rotor pole /electrode shape/overlapping length (mm): 96/96(1)/round/25, 96/96(2)/round/25, 96/80/round/25, 96/64/round/25, 96/48/round/25, respectively), as shown in Fig. 3, are researched.
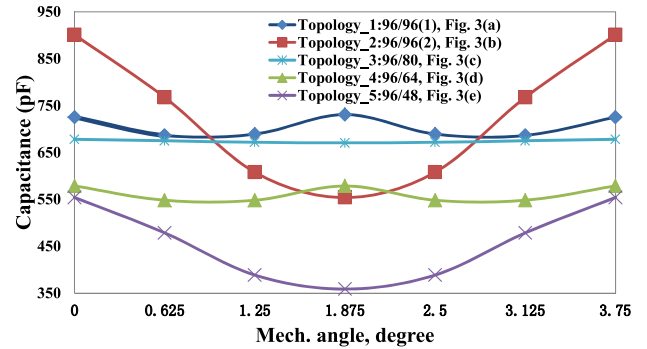

Fig. 4. Capacitances between stator 1 and rotor with different pole combinations.

The capacitances between stator 1 and rotor with different pole combination are compared in Fig. 4. Capacitances between stator 2 and rotor, which are 180° shifted in phase position compared with capacitance between stator 1 and rotor, are not shown in the Fig. 4. In order to research the influence of the relative position of two adjacent stator rows, the capacitances of two different topologies with the same stator pole/rotor pole combination of 96/96 are compared, as shown in Fig. 3(a) and (b). There is 180 electrical degree difference in location between two adjacent rows in Fig. 3(a), while 0 electrical degree difference in Fig. 3(b). The minimum airgaps between rotor and stator of the 5 topologies are all located at 0° position, where maximum capacitance lies, and the minimum capacitances of the five topologies lie at 0.9375°, 1.875°, 0.375°, 0.9375°, and 1.875° position, respectively. As can be seen, the distance over which the maximum and minimum capacitance occur of 96/96(1) topology is shorter than that of 96/96(2) topology, causing the capacitance variation of 96/96(1) topology is lower than that of 96/96(2) topology. The capacitances of the 96/96(2) topology and 96/48 topology reach maximum and minimum at the same position. However, the stator electrode number of 96/48 topology located at maximum capacitance position is only half of that of the 96/96(2) topology, causing the amplitude and variation of capacitance of 96/48 topology is lower than that of 96/96(2) topology. The same conclusion can be achieved between 96/96(1) topology and 96/64 topology. The amplitudes of capacitances of the 96/96 topology are higher than those of the 96/80 topology, 96/64 topology and the 96/48 topology due to more interacting electrodes. Therefore, the rule can be derived that the number of interacting electrodes influences the amplitude of the capacitance, and that the pole combinations and the relative position of two adjacent stator rows influence the distance over which the maximum and minimum capacitance occur, subsequently, the variation of the capacitance. The comparison result shows that the capacitance variation of the topology with the same stator pole/rotor pole number, as topology 2 shows, is the largest. Fig. 3(f) shows the topology with rectangle cross section electrodes, which will be discussed in Part C.

C. Optimal Design

The prototype machine is downsized to improve the power density and save the material. The stator plate outer radius
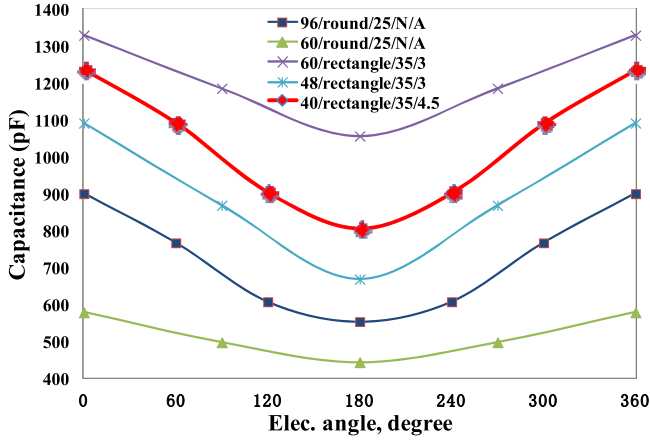
Fig. 5. Capacitances between stator 1 and rotor of different topologies.

TABLE II
PARAMETERS OF INITIAL DESIGN

Parameters	Rectangle electrode
Number of rows-stator	7
Number of rows-rotor	6
Electrode thickness	3 mm
Electrode overlapping length	35 mm
Minimum gap	1 mm
Row-to-row space	4 mm
Stator first row radius	50 mm
Stator plate outer radius	110 mm

Fig. 6. Performance comparison of the electrostatic machine and the induction machine.

decreased from 165 to 110 mm, and the minimum gap is enlarged from 0.5 to 1 mm to ensure that the processing technology can be achieved, while the variation of capacitance is also guaranteed. Optimum design is employed by comparing the capacitance of different topologies (pole number/electrode shape/overlapping length(mm)/span angle α (°) of 60/round/25/N/A, 60/rectangle/35/3, 48/rectangle/35/3, 40/rectangle/35/4.5, respectively). Rectangle electrodes are modified with round corners to avoid sharp edges resulting in breakdown event. Capacitances between the stator 1 and the rotor of different topologies are shown in Fig. 5, of which the variation of the capacitance of the 40/rectangle/35/4.5 topology, as shown in Fig. 3(f), is the largest. Compared with previous capacitance characteristic of the 96/round/25/N/A topology shown in Fig. 3(b), although the size of the motor and the electrode number are decreased and the minimum gap is enlarged, the better capacitance characteristic can be obtained by changing electrode shape from round to rectangle and increasing electrode overlapping length and span angle to increase the effective interaction area between the rotor electrode and stator electrode. Subsequently, the capacitance variation and torque density is guaranteed.

III. PROTOTYPE MACHINE CONSTRUCTION AND EXPERIMENT RESULTS

A. Prototype Machine Parameters

The parameters of the prototype motor with rectangle electrode are established based on the 40/rectangle/35 mm/4.5° topology, as shown in Table II.

Based on the simulated result of capacitance and (1), torque can be derived

$$T = V^2 \frac{\mathrm{d}}{\mathrm{d}x} C(x) = 4 \times 10^6 \times \frac{400 \times 10^{-12}}{6.28 \times 10^{-3}} = 0.25 \text{ N} \cdot \text{m} \tag{3}$$

where the voltage supplied V is assumed to be 2 kV. Speed of motor

$$n = \frac{60f}{P} = \frac{60 \times 5000}{40} = 7500 \text{ r/min} \tag{4}$$

where the frequency supplied f is assumed to be 5×10^3 Hz. Power of motor

$$P = \omega C V^2 = 50 \text{ W}. \tag{5}$$

The torque density of the prototype machine is 0.03 N·m/kg, which is comparable to the similar power level induction machines, e.g., the torque density of a 1/12 hp 1800 r/min 48 frame single phase induction machine is 0.04 N·m/kg [18]. As references for comparison, the torque of a 1/12 hp 1800 r/min 48 frame single phase induction machine is 0.34 N·m [18], and the maximum measured torque of a fluid-filled electrostatic machine is 0.7 N·m [17]. As can be seen, the torque of the proposed dielectric-gas-based electrostatic motor can reach the same order in magnitude with the fluid-filled electrostatic machine and induction machine at the similar power level. The prototype machine has a volume of 5.8 L and a mass of 4.58 kg. The torque density and power density with weight and volume of the prototype machine are 0.05 N·m/kg, 0.043 N·m/L, 10.9 W/kg and 8.6 W/L, respectively. The torque density and power density with weight and volume of the induction machine in [18] are 0.03 N·m/kg, 0.41 N·m/L, 9 W/kg, and 74.4 W/L, respectively. The radar chart, as Fig. 6 shows, compares the performance of the prototype machine with that of the induction machine. The data is converted into per-unit value to make the result more clearly. It appears that the torque density and power density with weight of the electrostatic motor are higher than that of the induction machine. However, the torque density and power density with volume of the prototype machine are much lower. In order to make the presented electrostatic motor more com-
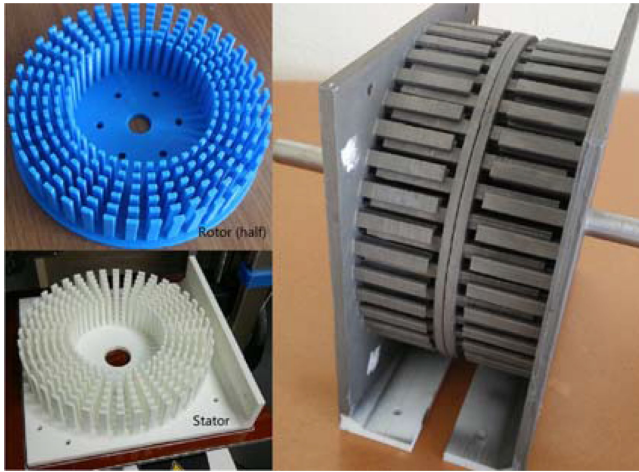
Fig. 7.   Prototype machine.

Fig. 8.   Comparison of predicted capacitance and measured capacitance.

petitive when volume is of primary concern, the torque density and power density with volume have to be increased, which can be realized by increasing the supplied voltage under UHV or insulating gas conditions.

B. Prototype Machine Construction

3-D printing is a process of creating 3-D objects using additive processes. Unlike material removed from a stock in the conventional machining process, 3-D printing builds a 3-D object from computer-aided design (CAD) model by successively adding material layer by layer. Thus, objects of almost any shape or geometry can be produced using 3-D printing. In order to eliminate the process of expensive mould manufacture, 3-D printing is used to validate the predicted results. As the electric field strength between electrodes is independent of the thickness of conducting layer, the prototype machine is printed in plastic and a thin layer of nickel is plated on the surface to make the prototype machine conductive. The 3-D printed rotor and stator using PLA plastic, as well as the prototype machine assembled, are shown in Fig. 7. For the future commercialized use, metallic motor will be produced to reduce the cost and manufacturing time.

C. Experiment Results

Comparison of predicted capacitance and measured capacitance is shown in Fig. 8. As can be seen, good agreement is achieved. The slightly difference between the measured result and the predicted result may be due to the errors in manufacture technology. The comparison result validates the design and optimization process of the presented dielectric-gas-based single-phase electrostatic motor.

As the drive of the motor is still in development, just stall torque is measured. The prototype machine, a stepper motor, and a torque sensor are fixed on the same axis through the coupling. First, the input pulse moves the stepper motor through a fixed angle, and the stepper motor is self-locked by the holding torque. Then voltage is applied to the prototype machine, and the generated torque acting on the torque sensor can be measured.
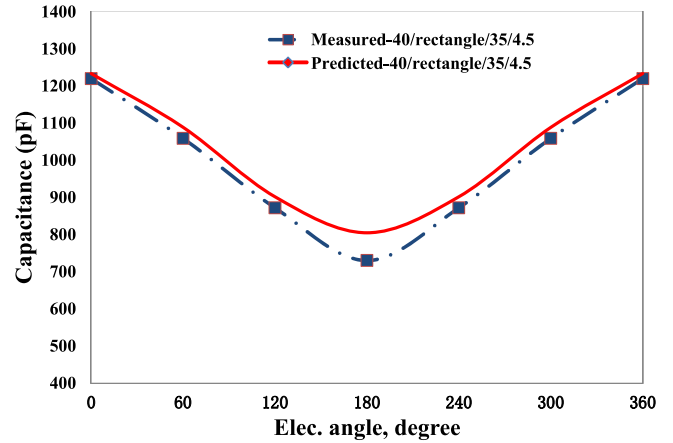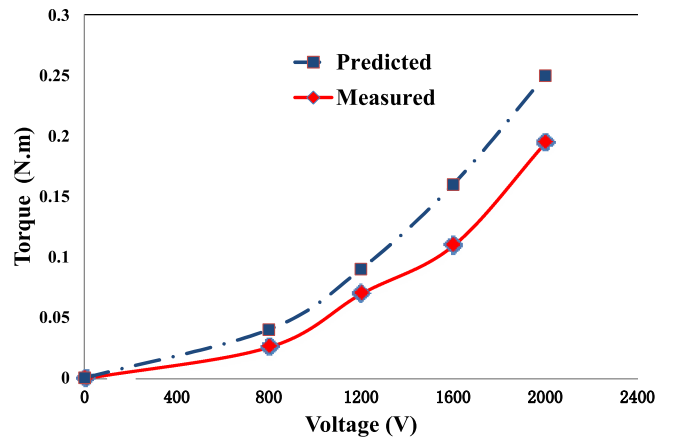

Fig. 9.   Comparison of predicted torque and measured torque.

The stepper motor is rotated and self-locked in different positions so as to find the maximum torque position. The predicted torque and measured maximum torque versus voltage are compared in Fig. 9. The predicted result is about 24% higher than the measured data. The error may be caused by the idealized calculation model of torque and the measurement error.

IV. DISCUSS OF MACHINE PERFORMANCE

A. Loss Calculation

There is no copper loss in electrostatic motor by eliminating copper winding, and no iron loss by eliminating iron core and permanent magnets. Therefore, only friction loss, windage loss, and dielectric loss exist in electrostatic motor.

Friction loss of the rolling bearing can be obtained from empirical equation

$$P_{\text{friction}} = 0.15\frac{F}{d}v \times 10^{-5} = 0.11 \text{ W} \tag{6}$$

where F, d, v are the load, diameter, and speed of the bearing, respectively.

Dielectric loss quantifies a dielectric material's inherent dissipation of electromagnetic energy. It can be parameterized in terms of the corresponding loss tangent $\tan\delta$. According to [13], the $\tan\delta$ of PLA plastic is less than 0.01 at working frequency,
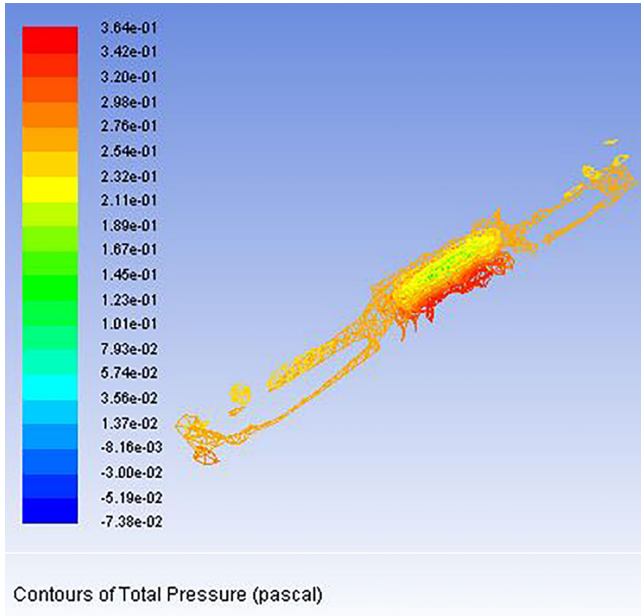
Fig. 10.   Pressure nephogram of one electrode.

so the dielectric loss can be estimates by

$$P_{\text{dielectric}} = \delta P = 0.5 \text{ W}. \tag{7}$$

Windage loss can be expressed as

$$P_{\text{windage}} = k C_f \pi \rho \omega^3 r^4 l \tag{8}$$

where k, ω, r, l are the surface roughness coefficient, angular speed, radius, and axis length of rotor, respectively. C_f, ρ are friction coefficient and density of air, respectively. However, friction coefficient of air is related to the shearing stress on the rotor surface, which depends on the fluent field condition and is difficult to calculate accurately. In this paper, 3-D fluent field simulation is performed to obtain the windage torque T_{Windage} first. The windage loss can be calculated by

$$P_{\text{windage}} = \frac{T_{\text{windage}} n}{9.56} \tag{9}$$

where the windage torque T_{Windage} is computed by adding the component caused by pressure force and the component caused by viscous force

$$T_{\text{windage}} = T_{\text{pressure}} + T_{\text{viscous}}. \tag{10}$$

The boundary conditions of the complete motor model are very complex and the simulation will consume a very long period. Therefore, the fluent field models of the electrodes in different rows are built respectively, and the total windage torque T_{Windage} is assumed to be the summation of windage torque of all the electrodes. For example, the analyzed pressure nephogram of one electrode is shown in Fig. 10.

Three boundary conditions are set as follows:
1) The boundary condition of fluent entrance is set as velocity inlet zone, and the boundary condition of fluent exit is set as pressure outlet zone.

TABLE III
MATERIAL THERMAL CONDUCTIVITY

Property	Thermal Conductivity (W/m/C)
Electrodes	237.5
Plates	237.5
Shaft	15
Bearing	4.5

2) The thermal boundary condition of the interface between solid component (electrode) and fluent component (air) is set as coupled zone.
3) The motion of the solid component (electrode) is set as rotation with speed of 7500 r/min.

The force can be obtained by the integration of pressure, and then the windage torque T_{Windage} about a specified center can be calculated. Finally, the windage loss obtained according to the (9) is 1.63 W.

B. Thermal Field Analysis

With the increasing requirements for reliability of electric machines, especially for those operating under formidable environment conditions, temperature rise becomes one of the most important design considerations of electric machines, particularly in permanent magnet machines since it may cause irreversible demagnetization of magnets. Finite element analysis (FEA) is a popular category in thermal analysis nowadays. This method can give thermal details in the conducting regions with different loss distributions, and any geometric shape can be modeled [14], [15]. In this paper, the thermal FEA analysis using ANSYS is performed to analyze the heat transfer characteristics of the presented electrostatic motor. Losses obtained in part A act as the heat source for the thermal field analysis.

The accuracy of FEA solution also requires the knowledge of thermal parameters of motor. The material of electrodes and plates is set as aluminum, and the materials of shaft and bearing are set as stainless steel and ceramics, respectively. Thermal parameters of the motor are shown in Table III.

Forced convective heat transfer between stator electrodes and rotor electrodes occurs when motor rotates. The convective heat transfer coefficient in the airgap is determined by the speed of motor, airgap length, and fluent field characteristic of air. Taylor number T_a, as shown in (11), is used to judge if the flow is laminar, vortex, or turbulent [16]

$$T_a = R_e \sqrt{\frac{\delta_g}{r_r}} \tag{11}$$

where δ_g is the airgap length, r_r is the rotor radius, R_e is the prandtl number, defined as the ratio of momentum diffusivity to thermal diffusivity, and can be expressed as:

$$R_e = \frac{\rho \upsilon \delta_g}{\mu} \tag{12}$$

where ρ is the fluid density (kg/m^3), υ is the fluid velocity (m/s), and μ is the fluid dynamic viscosity (kg/s.m). Taylor number of the prototype machine rotating at the speed of 7500 r/min can be calculated to be 1187, which is larger than 100, meaning that
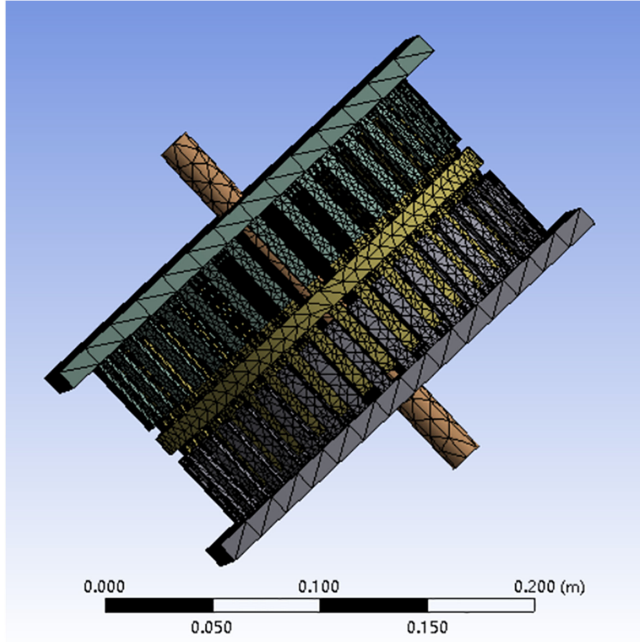
Fig. 11.   Meshes generated in the model.

the flow is fully turbulent and the Nusselt number reflecting heat transfer can be obtained by

$$N_u = 0.386T_a^{0.5}P_r^{0.27} \tag{13}$$

where P_r s the Prandtl number.

Consequently, the convective heat transfer coefficient in the airgap can be calculated by (14), and the result is 155 W/m^2/C

$$h = N_u \cdot \frac{\lambda_{\text{air}}}{2\delta_g} \tag{14}$$

where λ_{air} is the thermal conductivity of air.

Steady state thermal FEA is performed following the steps of building geometry, defining boundary condition, meshing, solving, and post processing. The size of mesh points in different parts of the machine should be set reasonably to satisfy the corresponding precision requirement. Meshed model with 1241047 elements generated is shown in Fig. 11.

Fig. 12 shows the temperature rise of the electrostatic motor at ambient temperature of 300 °C. The analyzed result reveals that the highest temperature of 346.1 °C lies in the rotor. The heat flux is higher and the heat dissipating environment is worse in the rotor, causing the temperature rise of the rotor is higher than that of the stator. As can be seen, the temperature rise of the machine is low and far below the melting point, meaning that the electrostatic motor presented can work stably at high ambient temperature, while irreversible damage of the magnets and the winding insulation of the electromagnetic motor will occur at such high ambient temperature.

C. Ultra-High Vacuum Condition Discuss

The analysis results reveal that the torque density with weight of the air-based prototype machine is comparable to the similar power level induction machines. However, the voltage supplied
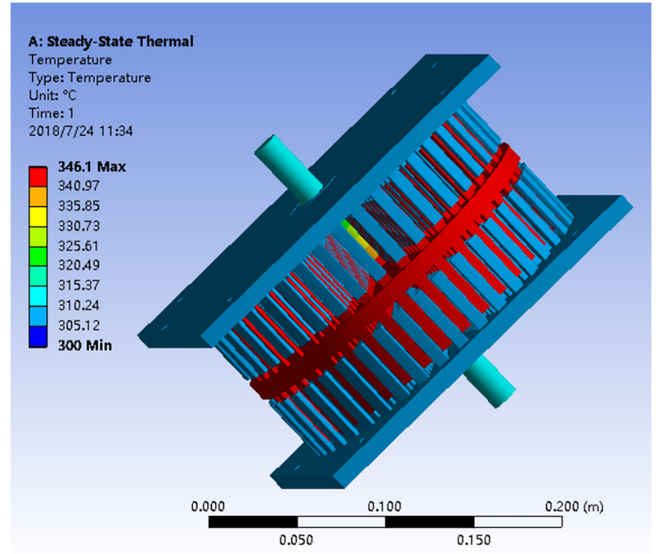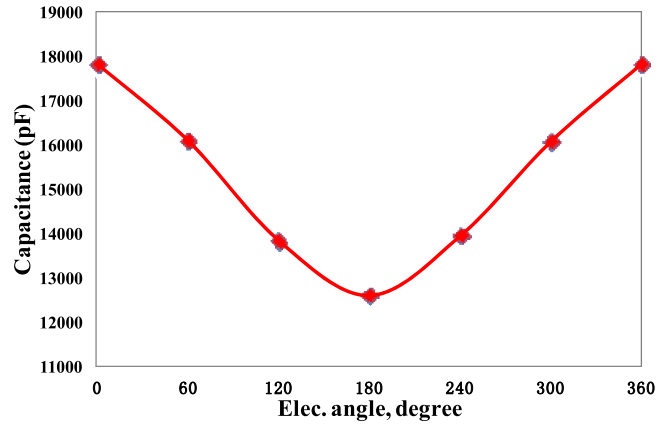

Fig. 12.   Temperature nephogram.

Fig. 13.   Predicted capacitances of 600 V voltage and 0.05 mm wide airgap.

is 2 kV, which is too high for industrial applications. Decreasing the width of airgap can increase the capacitance between stator and rotor, which means that lower voltage can be applied for the same output torque. It should be noted that decreasing the width of airgap leads to the decrease of breakdown voltage, e.g., the highest voltage applied to the 0.05 mm wide airgap is only 150 V considering the dielectric strength of air. Consequently, the output torque of motor is limited. Under UHV condition, the dielectric strength is enhanced, which means that higher voltage can be applied to ensure the output torque. The performance of the UHV-based motor under 600 V voltage and 0.05 mm wide airgap condition is analyzed. Predicted capacitance using FEA is shown in Fig. 13.

Output torque of the motor

$$T = V^2 \frac{\mathrm{d}}{\mathrm{d}x}C(x) = 0.36 \times 10^6 \times \frac{5225 \times 10^{-12}}{5.9 \times 10^{-3}} = 0.32 \, \text{N} \cdot \text{m} \tag{15}$$

where the voltage supplied V is assumed to be 600 V.

Speed of the motor

$$n = \frac{60f}{P} = \frac{60 \times 5000}{40} = 7500 \text{ r/min} \quad (16)$$

where the frequency supplied f is assumed to be 5×10^3 Hz.

Power of the motor

$$P = \omega C V^2 = 59 \text{ W}. \quad (17)$$

Compared with the performance of the air-based motor under 2 kV voltage and 0.1 mm wide airgap condition, the output torque, and power of the UHV-based motor under 600 V voltage and 0.05 mm wide airgap condition are increased, which means that higher voltage can be applied under UHV condition to ensure the output torque of the motor with smaller airgap. Therefore, UHV-based machine is a flexible structure for the dielectric-gas-based electrostatic motor.

V. CONCLUSION

In this paper, a dielectric-gas-based single-phase electrostatic motor is presented. Compared with previous liquid-filled and UHV works, two electric potentials of the single-phase electrostatic motor are distributed on two stators respectively, thus, stator plate is no need to be insulated for different potentials, which simplifies the construction and reduces the manufacture complexity. Optimization design is performed and an electrostatic motor with torque of 0.25 N·m, and power of 50 W is obtained. Achievable 3-D printing is used to build the prototype machine to eliminate the process of mould manufacture and achieve a weight reduction. Predicted capacitance of the machine is compared with measured result and good agreement is achieved. Thermal FEA analysis based on the losses calculated is performed at the ambient temperature of 300 °C, and the electrostatic motor presented can work stably. Future work includes drive design and performance testing of the electrostatic motor.

REFERENCES

[1] F. Lu, H. Zhang, H. Hofmann, and C. Mi, "An inductive and capacitive combined wireless power transfer system," *IEEE Trans. Power Electron.*, vol. 31, no. 12, pp. 8471–8482, Dec. 2016.
[2] F. Lu, H. Zhang, H. Hofmann, and C. Mi, "A double-sided LCLC-compensated capacitive power transfer system for electric vehicle charging," *IEEE Trans. Power Electron.*, vol. 30, no. 11, pp. 6011–6014, Nov. 2015.
[3] B. Q. Sun, F. T. Han, L. L. Li, and Q. P. Wu, "Rotation control and characterization of high-speed variable-capacitance micromotor supported on electrostatic bearing," *IEEE Trans. Ind. Electron.*, vol. 63, no. 7, pp. 4336–4345, Jul. 2016.
[4] A. Ketabi and M.J. Navardi, "Optimization of variable-capacitance micromotor using genetic algorithm," *J. Microelectromech Syst.*, vol. 20, no. 2, pp. 497–504, Feb. 2011.
[5] B. Ge and D. C. Ludois, "Design concepts for a fluid-filled three-phase axial-peg-style electrostatic rotating machine utilizing variable elastance," *IEEE Trans. Ind. Appl.*, vol. 52, no. 3, pp. 2156–2166, May 2016.
[6] B. Ge and D. C. Ludois, "Dielectric liquids for enhanced field force in macro scale direct drive electrostatic actuators and rotating machinery," *IEEE Trans. Dielectr. Electr. Insul.*, vol. 23, no. 4, pp. 1924–1934, Aug. 2016.
[7] B. Ge, D. C. Ludois, and A. N. Ghule, "A 3D printed fluid filled variable elastance electrostatic machine optimized with conformal mapping," in *Proc. IEEE Energy Convers. Congr. Expo.*, 2016, pp. 1–8.
[8] B. Ge and D. C. Ludois, "A 1-phase 48-pole axial peg style electrostatic rotating machine utilizing variable elastance," in *Proc. IEEE Int. Elect. Mach. Drives Conf.*, 2015, pp. 604–610.
[9] B. Ge and D. C. Ludois, "Evaluation of dielectric fluids for macro-scale electrostatic actuators and machinery," in *Proc. IEEE Energy Convers. Congr. Expo.*, 2014, pp. 1457–1464.
[10] R. O'Donnell, N. Schofield, A. C. Smith, and J. Cullen, "Design concepts for high-voltage variable-capacitance DC generators," *IEEE Trans. Ind. Appl.*, vol. 45, no. 5, pp. 1778–1784, Sep./Oct. 2009.
[11] T. Sashida, "Electrostatic motor," U.S. Patent 8278797 B2, Oct. 2, 2012.
[12] "Technology: High Power Electrostatic Motor–SHINSEI CORPORATION." 2015. [Online]. Available: http://www.shinsei-motor.com/English/techno/index.html.
[13] E. Huber, M. Mirzaee, J. Bjorgaard, M. Hoyack, S. Noghanian, and I. Chang, "Dielectric property measurement of PLA," in *Proc. IEEE Int. Conf. Electro Inform. Technol.*, 2016, pp. 0788–0792.
[14] N. Zhao and W. Liu, "Loss calculation and thermal analysis of surface-mounted PM motor and interior PM motor," *IEEE Trans. Magn.*, vol. 51, no. 11, pp. 1–4, Nov. 2015.
[15] N. Zhao, Z. Q. Zhu, and W. Liu, "Rotor eddy current loss calculation and thermal analysis of permanent magnet motor and generator," *IEEE Trans. Magn.*, vol. 47, no. 10, pp. 4199–4202, Oct. 2011.
[16] D. Staton, A. Boglietti, and A. Cavagnino, "Solving the more difficult aspects of electric motor thermal analysis in small and medium size industrial induction motors," *IEEE Trans. Energy Convers.*, vol. 20, no. 3, pp. 620–628, Sep. 2005.
[17] N. Zhao, F. Lu, H. Zhang, and C. Mi, "Design and optimization of a dielectric-gas-based single-phase electrostatic motor," in *Proc. Appl. Power Electron. Conf. Expo.*, 2018, pp. 3424–3437.
[18] "Marathon electric-Products Catalog." 2014. [Online]. Available: www.marathonelectric.com
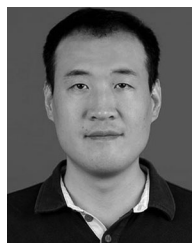
Nannan Zhao received the B.S., M.S., and Ph.D. degrees in electrical engineering from the Northwestern Polytechnical University, Xi'an, China, in 2005, 2008, and 2012, respectively.

He is currently an Associate Professor in Xi'an University of Architecture and Technology, Xi'an, China. His research interests include design theory and motion control technology of electrical machine.

Zihao Song received the B.S degree in electrical engineering from Nanjing University of Science and Technology, ZiJin College, Nanjing, China, in 2018. He is currently working toward the M.S degree in electrical engineering at Xi'an University of Architecture and Technology, Xi'an, China.

His research interests include analysis and computing of electrostatic field.

Zhengxu Li received the B.S degree in electrical engineering from Lishui University, Lishui, China, in 2017. He is currently working toward the the M.S degree in electrical engineering at Xi'an University of Architecture and Technology, Xi'an, China.

His research interests include design and optimization of electrical machines.
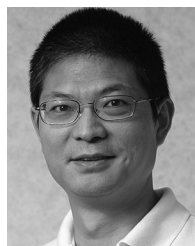
Nuo Shi received the B.S degree in electrical engineering from Xi'an University of Architectural Science and Technology Huaqing College, Xi'an, China, in 2018. He is currently working toward the M.S degree in electrical engineering at Xi'an University of Architecture and Technology, Xi'an, China.

His research interests include design and analysis of electrical machines.

Fei Lu (S'12–M'17) received the B.S. and M.S. degrees from the Harbin Institute of Technology, Harbin, China, in 2010 and 2012, respectively, and the Ph.D. degree from the University of Michigan, Ann Arbor, MI, USA, in 2017, all in electrical engineering.

He is currently an Assistant Professor in the Department of Electrical and Computer Engineering, Drexel University, Philadelphia, PA, USA. His research topic focuses on power electronics and the application of electric vehicle charging.

Chris Mi (S'00–A'01–M'01–SM'03–F'12) received the B.S.E.E. and M.S.E.E. degrees in electrical engineering from Northwestern Polytechnical University, Xi'an, China, and the Ph.D. degree in electrical engineering from the University of Toronto, Toronto, Ontario, Canada, in 1985, 1988, and 2001, respectively.

He is a Professor of electrical and computer engineering and the Director of the Department of Energy (DOE) -funded Graduate Automotive Technology Education (GATE) Center for Electric Drive Transportation, San Diego State University. His research interests include electric drives, power electronics, electric machines, renewable-energy systems, electrical and hybrid vehicles, battery management systems, and wireless power transfer.

Dr. Mi is a Fellow of SAE.

Hua Zhang (S'14–M'17) received the B.S., M.S., and Ph.D. degrees in electrical engineering from Northwestern Polytechnical University, Xi'an, China, in 2011, 2014, and 2017, respectively.

From September 2014 to August 2015, she was a joint Ph.D. student funded by the China Scholarship Council with the University of Michigan, Dearborn. From September 2015, she started to work in San Diego State University. She is currently a Postdoctoral Research Associate in Drexel University, PA, USA. Her research is about the charging technology of electric vehicles.

Weiguo Liu (SM'07) received the B.S. degree in electrical engineering from the Huazhong University of Science and Technology, Wuhan, China, and the M.S. degree in electrical engineering from the Northwestern Polytechnical University, Xi'an, China, and the Ph.D. degree in control theory and control engineering from the Northwestern Polytechnical University, Xi'an, China, in 1982, 1988, and 1999, respectively.

He is currently a Professor in Northwestern Polytechnical University, Xi'an, China. His research interests include design, intelligence control, and measurement of electrical machines.